Next-to-leading order QCD corrections to W^+W^+ and W^-W^- production in association with two jets

Francisco Campanario,[1,*] Matthias Kerner,[2,†] Le Duc Ninh,[2,3,‡] and Dieter Zeppenfeld[2,§]

[1]*Theory Division, IFIC, University of Valencia-CSIC, E-46980 Paterna, Valencia, Spain*
[2]*Institute for Theoretical Physics, KIT, 76128 Karlsruhe, Germany*
[3]*Institute of Physics, Vietnam Academy of Science and Technology,*
10 Dao Tan, Ba Dinh, 10000 Hanoi, Vietnam

We present a study of W^+W^+jj and W^-W^-jj production including leptonic decays in hadron-hadron collisions. The full electroweak and QCD induced contributions and their interferences are calculated at leading order. We find that, for inclusive cuts, the interference effects can be large if the jets are produced with large transverse momentum where, however, the production rate is suppressed. We also discuss the vector-boson-fusion cuts and show the validity of the vector-boson-fusion approximation. The next-to-leading order QCD corrections to the QCD-induced channels are also calculated. Compared to the previous calculation, we allow the intermediate W bosons to be off shell. For on-shell W production, we obtain an excellent agreement with previous results. Our code will be publicly available as part of the parton level Monte Carlo program VBFLNO.

I. INTRODUCTION

The production processes of two vector bosons in association with two jets at the LHC are important since they allow us to probe vector boson scattering and are sensitive to triple and quartic gauge couplings. In addition, they are also backgrounds to various searches for beyond the standard model physics. Their production can be classified into two groups, namely the electroweak (EW) induced channels of order $\mathcal{O}(\alpha^6)$ and the QCD-induced processes of order $\mathcal{O}(\alpha_s^2\alpha^4)$. Moreover, the EW contributions are divided into the t- and u-channels named vector-boson-fusion (VBF) mechanisms and the s-channel corresponding to the production of three EW gauge bosons with one off-shell gauge boson decaying into a quark-antiquark pair. The VBF processes, including in particular $VV \to VV$ scattering, have been calculated at next-to-leading order (NLO) QCD in Refs. [1–5] for all combinations of massive gauge bosons. A similar calculation with a W boson and a real photon in the final state has been done in Ref. [6]. NLO QCD corrections to triboson production including leptonic decays were computed in Refs. [7–12] and are available via the VBFNLO program [13] (see also Refs. [14–16] for on-shell production and Ref. [17] for NLO EW corrections).

NLO QCD calculations of the QCD-induced processes involving nontrivial color structures and the calculation of up to six-point one-loop integrals are more challenging. These calculations have been done for W^+W^+jj [18],

W^+W^-jj [19,20], $W^{\pm}Zjj$ [21] and $\gamma\gamma jj$ [22] production. The calculations of Refs. [4,18] have been implemented in the POWHEG BOX framework [23] as described in Refs. [24,25] for the W^+W^+jj channel. This implementation showed that the computing-time cost due to the calculation of the virtual corrections to the QCD-induced processes is a practical bottleneck [24].

The signature with same-charge W bosons is interesting because the backgrounds are small and it is related to the issue of double-parton scatterings. In this paper, we provide another independent calculation of the NLO QCD corrections to the QCD-induced W^+W^+jj and W^-W^-jj processes. Compared to the previous study presented in Ref. [18], we also include the off-shell gauge boson contribution and the gluon self-energy correction with a top quark in the loop. The importance of interference effects between the EW and QCD induced channels is a frequently asked question when studying vector boson pair production in association with two jets. These interferences are most important for the processes considered here due to the absence of gluon induced processes at leading order (LO) and since only left-chiral quarks contribute to the EW as well as QCD mechanisms. We discuss these effects at LO and expect that the results can be used as an upper limit for other $VVjj$ processes. We also aim at having a very fast code to solve the above computing-time problem. The code will be publicly available as part of the parton level Monte Carlo program VBFNLO.

This paper is organized as follows. In the next section, details of our calculation and code implementation are given. Numerical results are presented in Sec. III and the conclusions in the last section. Finally, in the appendix we provide results at the amplitude squared level at a random phase-space point to facilitate comparisons with our results.

*francisco.campanario@ific.uv.es
†matthias.kerner@kit.edu
‡duc.le@kit.edu
§dieter.zeppenfeld@kit.edu

II. COMPUTATIONAL DETAILS

As always done in the VBFNLO program, the leptonic decays of the EW gauge bosons are consistently included, with all off-shell effects and spin correlations taken into account. In the following, we consider the specific leptonic final state $e^+\nu_e\mu^+\nu_\mu$ and $e^-\bar{\nu}_e\mu^-\bar{\nu}_\mu$. The total results for all possible decay channels (i.e., $e^+\nu_e\mu^+\nu_\mu$, $e^+\nu_e e^+\nu_e$, $\mu^+\nu_\mu\mu^+\nu_\mu$ in the W^+W^+jj case and accordingly for the W^-W^-jj production) can, apart from negligible identical lepton interference effects, be obtained by multiplying our predictions by a factor two. For simplicity, we choose to describe the resonating $W^\pm$ propagators with a fixed width and keep the weak-mixing angle real.

A special feature of this process is that there are no subprocesses with external gluons at LO. All tree-level Feynman diagrams have two quark lines with a W boson attached to each, as displayed in Fig. 1. As a consequence, the total cross section without any cuts is finite at LO. Crossing symmetry is used to obtain, for two generations of quarks, all 20 subprocesses from the minimal set of two generic subprocesses (one subprocess involves same-generation quarks such as $u\bar{d}\to\bar{u}dW^+W^+$ and the other with different-generation quarks such as $u\bar{d}\to\bar{c}sW^+W^+$). It is obvious that the subprocesses with same-generation quarks are more complicated and include all diagrams of the different-generation subprocesses as a half set. This feature is used to avoid calculating the same diagrams twice. At NLO, there are the virtual and the real corrections. Figure 2 shows some selected contributions to the virtual
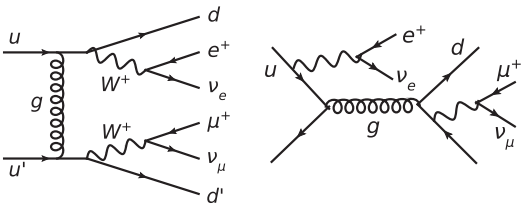

FIG. 1. Representative tree-level Feynman diagrams of the QCD-induced mechanisms for the process $pp\to e^+\nu_e\mu^+\nu_\mu jj$.
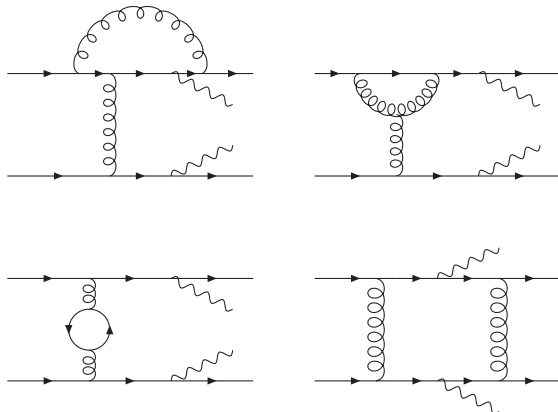

FIG. 2. Diagram types contributing to the virtual amplitude.

amplitude, which involves, in particular, the hexagon diagrams. The most difficult part of the calculation is computing the virtual amplitudes with up to six-point rank-four one-loop tensor integrals. There are eight six-point diagrams for each of four independent subprocesses with same generation quarks. For different generation quarks there are four six-point diagrams for six independent subprocesses. The calculation of tensor integrals is done using Passarino-Veltman reduction [26] for up to 4-point diagrams and the method of Ref. [27] (see also Refs. [28,29]) for higher-point tensor integrals. The scalar integrals are calculated as in Refs. [30–34]. The real emission contribution includes, for two generations of quarks, 36 subprocesses with seven particles in the final state. After removing the UV divergences in the virtual amplitude by the renormalization of α_s, both the virtual and real corrections are separately infrared divergent. These divergences cancel in the sum for infrared-safe observables such as the inclusive cross section and jet distributions. We use the dimensional regularization method [35] to regularize the UV and the infrared divergences and use an anticommuting prescription of γ_5 [36]. The virtual and real emission contributions are combined using the Catani-Seymour dipole subtraction algorithm [37].

We have constructed two independent implementations of the above described method. The results of the two computer codes are in full agreement, typically 10 to 12 digits with double precision, at the amplitude level for all subprocesses at NLO. The integrated part of the dipole subtraction term in Ref. [37] has been compared at the integration level. Moreover, we have also compared to the results of Ref. [18] using their settings and found a very good agreement. The first implementation is done in the VBFNLO framework [13], which will be described below. The second implementation uses FEYNARTS-3.4 [38] and FORMCALC-6.2 [39] to obtain the virtual amplitudes. The scalar and tensor one-loop integrals are evaluated with the in-house library LOOPINTS. The tree-level amplitudes for both LO and NLO real emission contributions are calculated in an optimized way using HELAS [40,41] routines.

In the following, we sketch the main implementation which has been added to the VBFNLO program and will be made public. We use the spinor-helicity formalism of Ref. [42] throughout the code. The virtual amplitudes can be classified into four different topologies as depicted in Fig. 2. They are evaluated with the use of five generic building blocks as described below. The upper diagrams of Fig. 2, which contain loop corrections to a quark line and are often called "bosonic" contributions, include sets of loop corrections to Born topologies with a fixed number and a fixed order of external particles. They are classified into Abelian and non-Abelian contributions. The first ones are computed with the so-called "boxline" depicted in Fig. 3. We use the effective current approach, thus, J_1 and J_2 should be understood as generic off-shell currents which
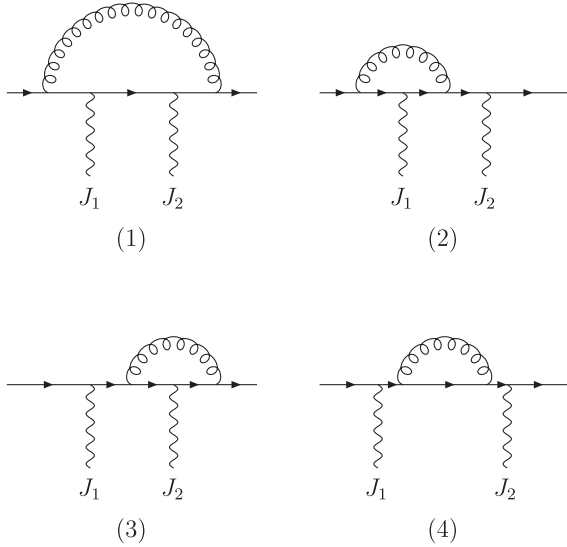
FIG. 3. Contributions of the Abelian boxline.

FIG. 5. Self-energy contributions to the amplitude.

can be either a W boson including the leptonic decays or a gluon connecting to the second quark line. The color factors associated with the individual diagrams are proportional to $C_F - C_A/2$ or C_F depending on whether the effective gluon is attached to the loop. For example, if J_1 is a gluon then it is $C_F - C_A/2$ for the first and second diagrams and C_F for the other ones.

Corrections to a quark line containing non-Abelian triple vertices are computed with the so-called "BoxlineNoAbe" building block depicted in Fig. 4. g^* and J_1 represent again generic effective currents to which the building block can be contracted. These building blocks have been extensively checked in Ref. [28] and used in other VBFNLO processes. The self-energy corrections, which are illustrated in the bottom left diagram of Fig. 2 and include various contributions shown in Fig. 5, form another building block. We note that the top-loop corrections are included.

Finally, there are building blocks involving from hexagon to box corrections with two quark lines directly attached to the loop as illustrated in the bottom right diagram of Fig. 2 and further shown in Fig. 6. They are
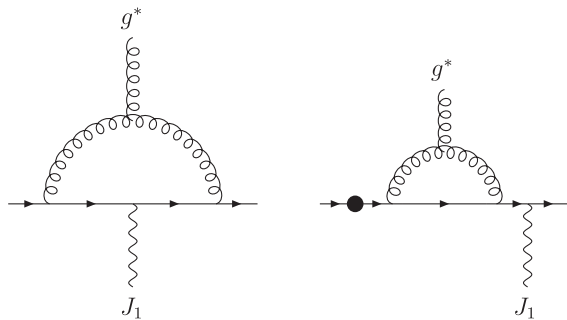
gathered in EW gauge invariant subsets and named "hexbox" contributions. The first subset depicted in Fig. 6 consists of nine diagrams. The other subset is obtained by crossing the two gluon lines and constitutes an independent group. To compute them, we generalized the software developed in Ref. [28] to be able to compute hexagon diagrams with two fermion lines. We use the Chisholm identities (see e.g. Ref. [43]), which reduces the CPU time required to evaluate the hexbox contributions by a factor ten.

While the color factors of the boxline and self-energy contributions are given by a constant times the color structure of the corresponding Born diagram, the hexbox diagrams involve a more complicated structure. For the diagrams shown in Fig. 6, it is given by

$$(T^b T^a)_{ji}(T^b T^a)_{lk} = -\frac{1}{6}T^a_{ji}T^a_{lk} + \frac{1}{2}T^a_{li}T^a_{jk}$$

$$= -\frac{1}{6}\mathcal{C}_t + \frac{1}{2}\mathcal{C}_u, \tag{1}$$

FIG. 4. Non-Abelian boxline contributions. The dot indicates the additional position, where the external boson can be attached.
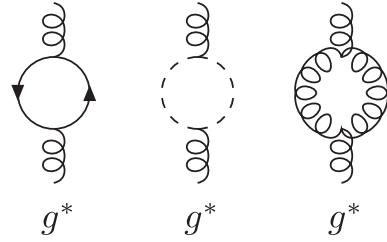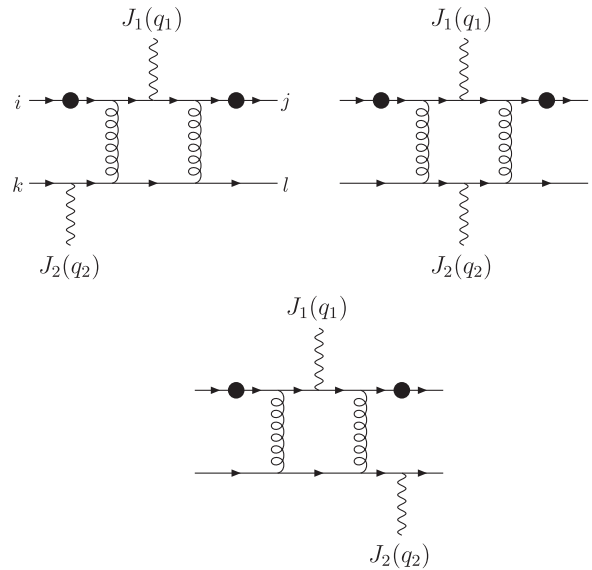

FIG. 6. Hexbox contributions. The dots indicate additional positions, where the external boson on the upper line has to be attached.

where $\mathcal{C}_t$ and $\mathcal{C}_u$ are the color structures of the corresponding t and u channel Born diagrams. The color factors of the hexbox diagrams with crossing gluons are

$$(T^a T^b)_{ji}(T^b T^a)_{lk} = \frac{4}{3}\mathcal{C}_t + \frac{1}{2}\mathcal{C}_u. \qquad (2)$$

After adding each Feynman diagram to the corresponding color structure(s), the squared amplitude can be calculated using

$$\begin{pmatrix} \mathcal{C}_t \\ \mathcal{C}_u \end{pmatrix}^* \cdot (\mathcal{C}_t \quad \mathcal{C}_u) = \begin{pmatrix} 2 & -\frac{2}{3} \\ -\frac{2}{3} & 2 \end{pmatrix}. \qquad (3)$$

We now discuss the issue of numerical instabilities and how to detect them. This is most relevant to the phase-space integration of the virtual contribution, which shows numerical cancellations in the calculation of one-loop tensor integrals. Our solution is described as follows. We use the Ward identities obtained by replacing an effective current with the corresponding momentum to relate N-point integrals to lower point integrals. Those identities are called gauge tests and are checked for every phase-space point with a small additional computing cost by using a cache system. The specific tests for the bosonic contributions can be found in Ref. [28]. Here, we concentrate on the hexbox contributions which are most complicated. The hexbox contributions vanish under the replacement $J_i(q_i) \to q_i$, because they form EW gauge invariant subsets. The gauge structure of these contributions is very rich. The subset of three diagrams of Fig. 6 (ignoring the dots), where the position of the external gauge boson in the upper quark line is fixed and all possible insertions in the lower line are considered, vanishes for $J_2(q_2) \to q_2$. Totally, we can construct up to 6 of such identities (three for the upper and three for the lower line), which are used to flag possible instabilities.

If a bad phase-space point is identified, i.e. the gauge tests are true by less than 2 digits with double precision, the point is discarded. For a typical calculation with the inclusive cuts specified below, the number of discarded points is statistically negligible. This strategy was also successfully applied for $W\gamma\gamma +$ jet and EW $Hjjj$ production at NLO QCD in Refs. [44,45] without further need of using any additional rescue system.

Finally, we have a few comments on code optimization and running time. Since the leptonic decays of the EW gauge bosons are common for all subprocesses, the VBFNLO approach is to calculate these decays once for each phase-space point and store them. Due to the large number of subprocesses, we extend this procedure and also precalculate parts of Feynman diagrams, that are common to the subprocesses of the real emission. In addition, a caching system to reuse Born amplitudes for different dipole terms [37] has been implemented. With this method, we obtain the NLO inclusive cross section with statistical error of 1%

in half an hour on an Intel i5-3470 computer with one core and using the compiler Intel-ifort version 12.1.0.

III. NUMERICAL RESULTS

We choose $M_W = 80.385$ GeV, $M_Z = 91.1876$ GeV, $M_H = 126$ GeV and $G_F = 1.16637 \times 10^{-5}$ GeV^{-2} as EW input parameters and use the MSTW2008 parton distribution functions [46] with $\alpha_s^{\mathrm{LO}}(M_Z) = 0.13939$ and $\alpha_s^{\mathrm{NLO}}(M_Z) = 0.12018$. Quark mixing effects are neglected and all the fermions, except the top quark with $m_t = 173.1$ GeV, are treated as massless. From this, we get $\Gamma_W = 2.09761$ GeV, $\Gamma_Z = 2.5089$ GeV and $\Gamma_H = 4.195$ MeV. We work in the five-flavor scheme and use the $\overline{\mathrm{MS}}$ renormalization of the strong coupling constant with the top quark decoupled from the running of α_s. However, the top-loop contribution is explicitly included in the virtual amplitude. Subprocesses with external third generation quarks should be treated as different processes and are therefore excluded.

We define the inclusive cuts as follows

$$p_{T(j,l)} > 20 \text{ GeV} \qquad \not{p}_T > 30 \text{ GeV}$$
$$|y_j| < 4.5 \qquad |y_l| < 2.5 \qquad R_{l(l,j)} > 0.4. \qquad (4)$$

The jets are clustered using the anti-k_t algorithm [47] with a cone radius of $R = 0.4$. We use a dynamical factorization and renormalization scale with the central value

$$\mu_0 = \frac{1}{2}\left(\sum_{\mathrm{partons}} p_{T,i} + \sum_{W_i} \sqrt{p_{T,i}^2 + m_{W,i}^2}\right), \qquad (5)$$

where $m_{W,i}$ denotes the invariant mass of the corresponding leptons. This is our default scale choice if not otherwise stated.

A. Full LO results

We consider the full LO contribution including both the EW-induced and the QCD-induced channels and ask the following questions: (i) are the interference effects between the EW-induced and the QCD-induced mechanisms important? (ii) what are the cuts for the VBF contribution to be dominant? To answer these questions, the full LO cross section is divided into various contributions: the QCD-induced contribution of order $\mathcal{O}(\alpha_s^2 \alpha^4)$, the full EW-induced contribution including the t, u and s channel diagrams as shown in Fig. 7 of order $\mathcal{O}(\alpha^6)$ and the interference contribution of order $\mathcal{O}(\alpha_s \alpha^5)$. The VBF contribution of order $\mathcal{O}(\alpha^6)$ includes only t and u channels. The VBF approximation, as implemented in the VBFNLO program, neglects the interference effects between the t and u channels for processes with two identical quark lines. This has been shown to be a very good approximation if VBF cuts are applied, see e.g. Ref. [5]. Hereafter, results of the VBF contribution are calculated using the VBF
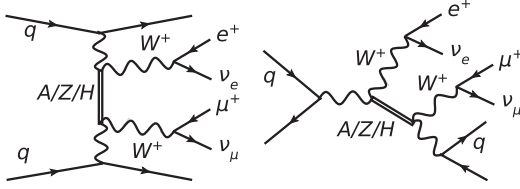
FIG. 7. Representative tree-level Feynman diagrams of the EW-induced mechanisms for the process $pp \to e^+\nu_e\mu^+\nu_\mu jj$. The double lines represent either a neutral EW gauge boson or the Higgs.

approximation. In Fig. 8 we show those various contributions as functions of the transverse momentum (top row panels) and invariant mass (bottom left panel) of the two tagging jets ordered by p_T. The distributions of the rapidity separation between the two jets are also displayed in the bottom right panel. Here we define $\Delta y_{\text{tags}} = |y_{j1} - y_{j2}|$.

The relative EW, QCD and interference contributions compared to the full LO results are also plotted in the small panels. Our results obtained by using the VBFNLO framework have been cross checked against the program SHERPA [48] using the COMIX [49] matrix element generator. Results at the cross section level for those contributions with different cuts are given in Table I. The loose VBF cuts include the inclusive cuts and two additional cuts

$$m_{jj} > 200 \text{ GeV}, \qquad \Delta y_{\text{tags}} > 2.5. \qquad (6)$$

The tight VBF cuts are the inclusive cuts together with

$$m_{jj} > 500 \text{ GeV}, \qquad \Delta y_{\text{tags}} > 4, \qquad y_{j1} \cdot y_{j2} < 0, \qquad (7)$$

and the charged leptons must be in the rapidity gap of the two tagging jets.
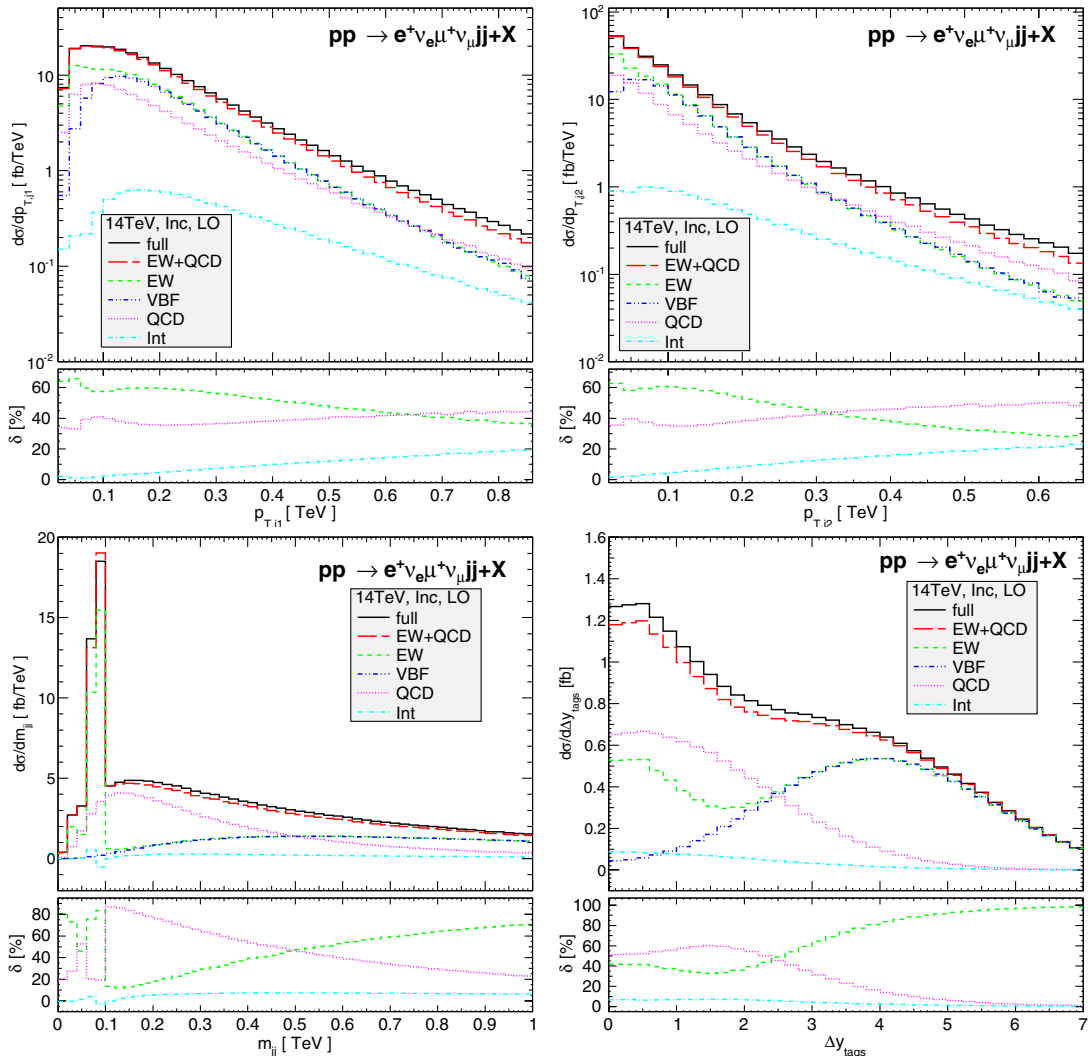

FIG. 8 (color online). Differential cross sections with inclusive cuts for the transverse momenta (top row) and the invariant mass (bottom left) of the two tagging jets ordered by p_T. The distributions of the rapidity separation between the two jets are in the bottom right panel. The relative EW, QCD and interference contributions compared to the full LO results are also plotted in the small panels.

TABLE I. LO cross sections (in fb) for various contributions with different cuts as defined in the text. The statistical errors are below 1 ab.

	VBF	EW	QCD	Int	Full
Inclusive	2.189	2.784	1.810	0.234	4.828
Loose VBF	1.784	1.783	0.362	0.058	2.203
Tight VBF	0.971	0.970	0.040	0.013	1.023

The numerical results for the inclusive cuts tell us that the interference effect between the QCD and EW induced channels is largest when the jets are produced with large p_T and when Δy_{tags} is small. The transverse momentum distributions show a steady increase of this effect, reaching about 20% for $p_{T,j1}$ about 800 GeV or $p_{T,j2}$ about 600 GeV. It reduces to below 10% (3%) for the loose (tight) VBF cuts. For the Δy_{tags} distribution, the effect is almost constant for small separation, about 6%, and then gradually decreases for $\Delta y_{\text{tags}} > 2$. The interference effect is more democratic in the m_{jj} distribution, about 6% for a large range of $m_{jj} > 300$ GeV. We have also looked at the $p_{T,l}$, with $l = e^+, \mu^+$, and the m_{ll} distributions (not shown) and observed that the effect is always smaller than 6%, being largest in the low energy regime. Thus, the interference effect can be large in the $p_{T,j}$ distributions at high transverse momentum. However, in this phase space region, the cross section is suppressed. Moreover, there is another well-known effect of EW Sudakov corrections due to the exchange of a massive gauge boson in loop diagrams, which can introduce negative corrections of about -5% at $p_{T,j} \approx 800$ GeV, see e.g. Ref. [50].

Figure 8 and Table I show also other interesting features of the QCD and EW mechanisms. Their contributions are of the same level despite the hierarchy of the coupling constants. The reason is that the EW mechanisms are more dynamically enhanced compared to the QCD mechanism. For instance, the s channel diagram in Fig. 7 can have simultaneously three resonating W propagators, dominating in the region of small $m_{jj} \approx 80$ GeV. The VBF contribution including only t and u channels dominates at large m_{jj} and large Δy_{tags}. For the inclusive cross section, the VBF contribution is slightly larger than the QCD one. This is because initial and final state W emissions interfere destructively for QCD-induced processes in the central region, which is kinematically favored due to the substantial mass of the W bosons. This suppression does not occur in the VBF channels because of an additional sign flip in the EW charge between the initial and final state W emissions. Therefore, if we want to observe the VBF signature, then we can impose loose or tight VBF cuts as defined in Eq. (6) and Eq. (7), respectively. The QCD contribution to the cross section reduces from 37% for the inclusive cuts to 16% (4%) for loose (tight) VBF cuts. The effects of the VBF cuts are twofold: reducing the QCD-induced contribution and improving the VBF

approximation. With these cuts, we can obtain a very good prediction using the VBF approximation at NLO QCD, the QCD-induced contribution at NLO QCD and the interference terms calculated at LO. However, if one wants to have more events with same-charge W bosons, then measurements with inclusive cuts should also be considered. In this context, NLO QCD corrections to the QCD-induced channels are more important; this is the topic of the next section. We note that the full EW contribution at LO has been calculated in Ref. [5] with slightly different VBF cuts and a different scale choice. Despite these differences, we can see that their results are consistent with ours.

B. NLO QCD results for the QCD-induced channels

We now focus on the inclusive cuts and study the NLO QCD corrections to the QCD-induced channels. The dependence of the cross section on the scales μ_F and μ_R, which are set equal for simplicity, is shown in Fig. 9. The central value μ_0 is defined in Eq. (5). As expected, we observe a significant reduction in the scale dependence around μ_0 when the NLO contribution is included. The uncertainties obtained by varying $\mu_{F,R}$ by factors 1/2 and 2 around the central value are 45% (45%) at LO and 16% (18%) at NLO for the W^+W^+ (W^-W^-) channel. At $\mu = \mu_0$, we get $\sigma_{\text{LO}} = 1.81^{+0.47}_{-0.34}$ fb ($0.90^{+0.23}_{-0.17}$ fb) and $\sigma_{\text{NLO}} = 2.17^{+0.15}_{-0.19}$ fb ($1.13^{+0.10}_{-0.10}$ fb). By varying the two scales separately, we observe a small dependence on μ_F, while the μ_R dependence is similar to the behavior shown in Fig. 9.

To understand the phase-space dependence of the NLO QCD corrections, we plot, for the W^+W^+ case, in Fig. 10
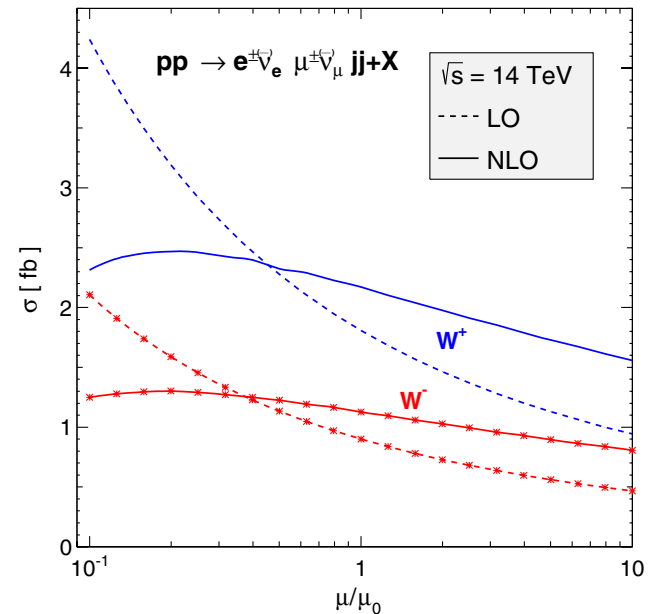

FIG. 9 (color online). Scale dependence of the LO and NLO cross sections at the LHC. The curves with and without stars are for W^-W^-jj and W^+W^+jj productions, respectively.
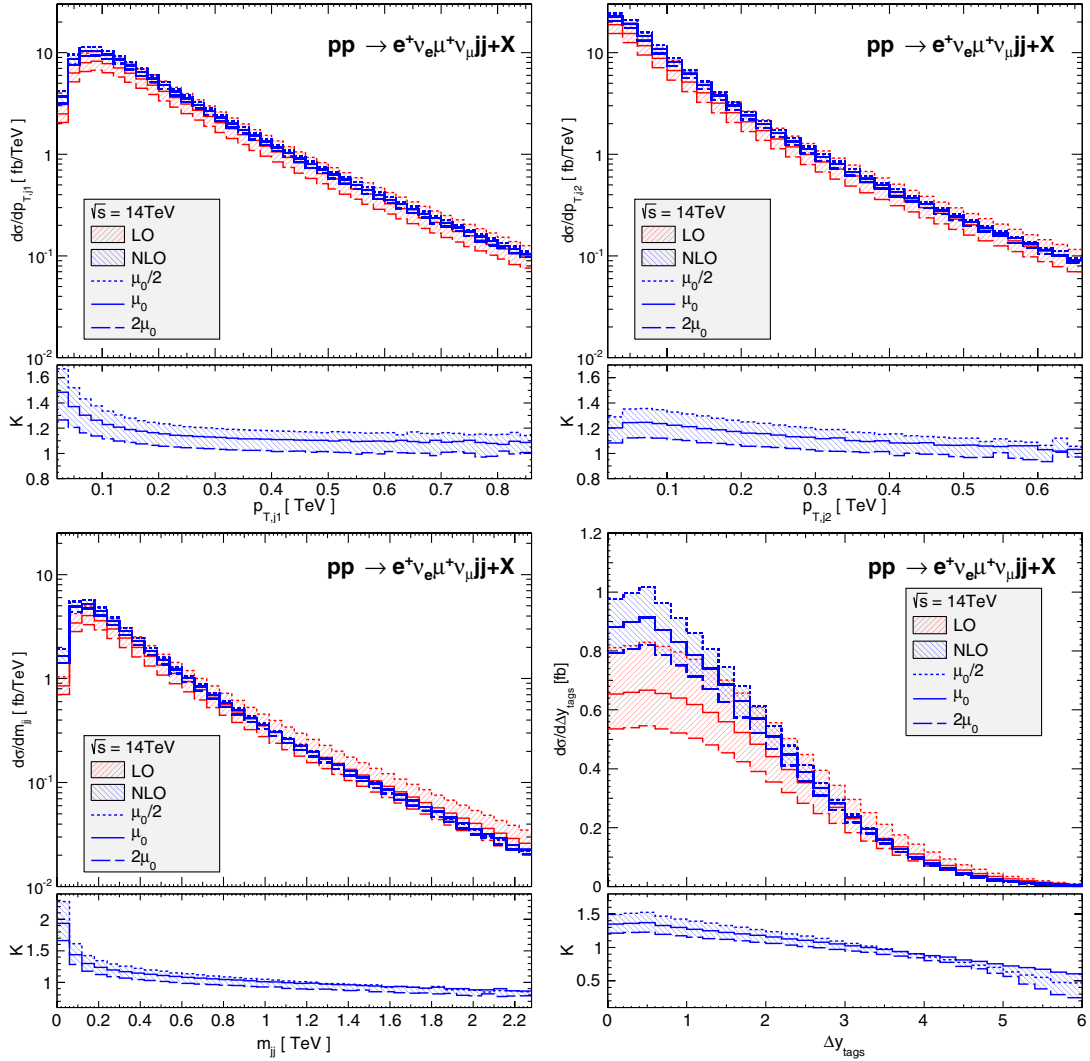
FIG. 10 (color online).   Differential cross sections, for the QCD-induced channels at LO and NLO, with inclusive cuts for the transverse momenta (top row) and the invariant mass (bottom left) of the two tagging jets ordered by p_T. The distributions of the rapidity separation between the two jets are in the bottom right panel. The bands describe $\mu_0/2 \leq \mu_F = \mu_R \leq 2\mu_0$ variations. The K-factor bands are due to the scale variations of the NLO results, with respect to $\sigma_{LO}(\mu_0)$. The solid lines are for the central scale while the dotted and dashed lines correspond to $\mu_0/2$ and $2\mu_0$, respectively.

the differential cross sections for the transverse momenta (top row) and the invariant mass (bottom left) of the two tagging jets ordered by p_T as in the previous section. The distributions of the rapidity separation between the two jets are in the bottom right panel. The K factors, defined as the ratio of the NLO to the LO results, are shown in the small panels. The distributions at NLO are much less sensitive to the variation of the scales than at LO. We observe nontrivial phase-space dependence of the K factors. It varies, for $\mu = \mu_0$, from 1.5 to 1.1 for the p_T distribution of the hardest jet and from 1.2 to 1 for the second hardest jet in a large energy range up to about 700 GeV.

A more striking dependence is found in the Δy_{tags} distributions. The K factor is about 1.5 at $\Delta y_{\text{tags}} = 0.5$ and decreases rapidly with large rapidity separation

between the two tagging jets. The QCD correction changes sign at about $\Delta y_{\text{tags}} = 3.3$ and the scale uncertainty band of the K factor has a minimum width at about 4, blowing up with further increasing jet separation. This is probably because the invariant mass m_{jj} rapidly increases at large Δy_{tags}, while the tagging jets are mainly produced with low p_T,

$$m_{jj}^2 \approx 2p_{T,j1}p_{T,j2}[\cosh(y_{j1} - y_{j2}) - \cos(\phi_{j1} - \phi_{j2})]. \quad (8)$$

Note that $\cosh(\Delta y)$ inflates from 1 at $\Delta y = 0$ to 27 at $\Delta y = 4$. The low value of $p_{T,j2}$ basically introduces a jet veto for further jet activities. This large difference between the values of m_{jj} and $p_{T,\text{veto}}$ leads to large QCD corrections. It then becomes clear that the dynamic scale μ_0 is too small
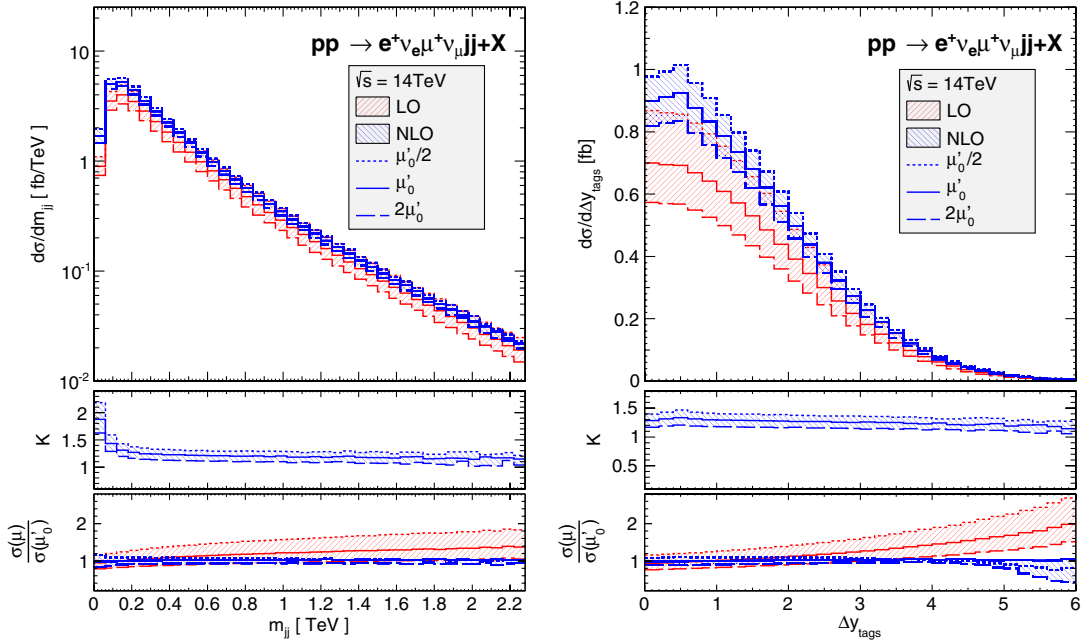
FIG. 11 (color online).   Similar to Fig. 10 but for the new scale choice $\mu_F = \mu_R = \mu_0'$ defined in Eq. (9). Additional panels at the bottom show the ratios of differential cross sections with the default scale μ_0 over the ones with μ_0' at LO and NLO. The bands on these ratios show the scale variations $\mu_0/2 < \mu < 2\mu_0$ of the numerators while the denominators are calculated at the central scale.

at large Δy_{tags} and the invariant mass m_{jj} should be taken into account in the scale choice. Using a larger scale would make the NLO result more stable and reduce the LO result, hence bringing the K factor closer to one as will be shown later.

The m_{jj} distribution shown in the bottom left plot in Fig. 10 does not exhibit the same behavior at large m_{jj}. The K factor is about one at 1 TeV and the uncertainty band is regular. At large m_{jj}, the dominant contribution comes from the configuration with small Δy_{tags} (see bottom right plot in Fig. 10) and large transverse momenta. Therefore, using μ_0 is reasonable here. However, an additional feature appears in the low energy regime where a large K factor occurs, being larger than 2 for $m_{jj} < 30$ GeV. At LO, there are two quark jets which are well separated because there is a finite IR cutoff due to the W mass. The m_{jj} distribution has a peak at about 150 GeV at LO. The peak's position is shifted to a smaller value at NLO, leading to a large K factor at small m_{jj}. This is due to a new kinematic configuration opening up at NLO, where a final-state quark splits into a quark-gluon pair, resulting in two jets with low invariant mass. The second quark can either be unobserved or be combined in the quark jet. We have explicitly verified this by computing the contribution separately.

The above discussion indicates that the choice of scales is not trivial and the best choice can be observable dependent, being more important for LO predictions as we will show. A better scale taking into account that m_{jj} can be much larger than the default scale μ_0, Eq. (5), when Δy_{tags} is large was proposed in Ref. [51] in the framework

of dijet production. To accommodate the vector bosons, we slightly modify it and propose

$$\mu_0' = \frac{1}{2} \left(\sum_{\text{jets}} p_{T,i} \exp |y_i - y_{12}| + \sum_{W_i} \sqrt{p_{T,i}^2 + m_{W,i}^2} \right), \quad (9)$$

where $y_{12} = (y_1 + y_2)/2$ denotes the average rapidity of the two hardest jets. The first contribution in this scale interpolates between $\sum_{\text{jets}} p_{T,i}/2$ and m_{jj}, so that μ_0' is approximately equal to μ_0 and m_{jj} for small and large Δy_{tags} values, respectively. New distributions with this scale choice are shown in Fig. 11 for Δy_{tags} and m_{jj}. The other $p_{T,j}$ distributions shown in Fig. 10 are not much affected and therefore not shown for the new scale. As expected, we observe that the K factor for the Δy_{tags} distribution becomes more regular, flatter and closer to one. The K factor for the m_{jj} distribution also gets flatter at large m_{jj}. Furthermore, in the lower panel where the ratio of the predictions of the two scales at LO and NLO are plotted, one can observe that the differences are mainly due to the changes of the LO predictions and the NLO are more stable. This points out the sensitivity of the LO prediction to different scale choices and the relevance of the NLO predictions to stabilize the results. These results justify the above argument about the shortcoming of the scale μ_0.

IV. CONCLUSIONS

In this paper, we have presented a study of the production of two equal-charge W bosons in association with two

jets at the LHC with 14 TeV center-of-mass energy. The full LO calculation has been done and it was found that the interference effects between the QCD-induced and EW-induced channels can be large if the jets are produced with high transverse momentum, reaching about 20% at $p_{T,j1} \approx 800$ GeV, for inclusive cuts. It reduces to below 3% for tight VBF cuts. The full LO results also show that the QCD-induced contribution is largely removed using VBF cuts.

We have also studied the QCD-induced channels at NLO QCD using the inclusive cuts. As expected, it was found that the inclusion of the QCD corrections reduces significantly the scale uncertainties of the cross section and of differential distributions. We have discussed the dependence of the QCD corrections on the kinematics of the two tagging jets for two different scale choices. For the $p_{T,j}$ distributions, the K factor for the central scale varies from 1 to 1.5 for a large energy range up to 800 GeV. The K factor of the invariant mass distribution is larger than 2 for $m_{jj} < 30$ GeV due to a new kinematic configuration opening up at NLO. For large invariant mass, $m_{jj} > 200$ GeV, the QCD correction is smaller than 20%. More interesting is the dependence on the rapidity separation between the two hardest jets. For our default scale μ_0, given by the sum of jet and W transverse energies, the K factor decreases steadily with increasing separation and becomes smaller than one for $\Delta y_{\text{tags}} > 3.3$. The scale uncertainty band has a minimum width at $\Delta y_{\text{tags}} = 4$ and then blows up with increasing jet separation. This is because the central scale μ_0 is too small compared to the hard scale m_{jj}, which typically is large for high Δy. This conclusion is justified by the results obtained using another scale μ_0', which takes into account m_{jj} for large jet separations. By choosing μ_0' the LO results are much closer to the NLO ones and the phase space

dependence of the K factors is strongly reduced for the observables shown in this article.

On a technical note, compared to the first calculation reported in Ref. [18], we allow the intermediate W bosons to be off shell and the top-loop contribution is included. Neglecting these small effects, we obtain a very good agreement with the results of Ref. [18], both at the amplitude squared and cross-section levels. Finally, our code will be publicly available as part of the VBFNLO program [13], therefore further studies of the QCD corrections with different kinematic cuts can be easily done.

ACKNOWLEDGMENTS

APPENDIX: RESULTS AT ONE PHASE-SPACE POINT

In this appendix, we provide results at a random phase-space point to facilitate comparisons with our results. The phase-space point for the process $q_1\bar{q}_2 \to \bar{q}_3 q_4 e^+ \nu_e \mu^+ \nu_\mu$ is given in Table II. In the following we provide the squared amplitude averaged over the initial-state helicities and colors. We also set $\alpha = \alpha_s = 1$ for simplicity. The top quark is decoupled from the running of α_s. However, its contribution is explicitly included in the one-loop amplitudes. At tree level, we have

TABLE II. Momenta (in GeV) at a random phase-space point for $q_1\bar{q}_2 \to \bar{q}_3 q_4 e^+ \nu_e \mu^+ \nu_\mu$ subprocesses.

	E	p_x	p_y	p_z
q_1	18.3459102072588	0.0	0.0	18.3459102072588
$\bar{q}_2$	4853.43796816526	0.0	0.0	−4853.43796816526
$\bar{q}_3$	235.795970274883	−57.9468743482139	$-7.096445419113396 \times 10^{-15}$	−228.564869022223
q_4	141.477229270568	−45.5048903376581	−65.9221967646567	−116.616359620580
e^+	276.004829895761	31.4878768361538	−8.65306166938040	−274.066240646098
ν_e	1909.28515244344	29.6334571080402	40.1409467910328	−1908.63311192893
μ^+	2241.46026948104	28.1723094714198	30.2470561132914	−2241.07910976778
ν_μ	67.7604270068059	14.1581212702582	4.18725552971283	−66.1323669723852

TABLE III. QCD interference amplitudes $2\,\text{Re}\,(\mathcal{A}_{\text{NLO}}\mathcal{A}_{\text{LO}}^*)$ for $u\bar{d} \to \bar{u}d e^+ \nu_e \mu^+ \nu_\mu$ subprocess.

	$1/\epsilon^2$	$1/\epsilon$	Finite
I operator	$1.053330833015670 \times 10^{-2}$	$-5.936404140457268 \times 10^{-3}$	$2.640293552481222 \times 10^{-3}$
Loop	$-1.053330833914469 \times 10^{-2}$	$5.936404145582775 \times 10^{-3}$	$8.079973631744798 \times 10^{-3}$
I+loop	$-8.987987823141610 \times 10^{-12}$	$5.125507271694671 \times 10^{-12}$	$1.072026718422602 \times 10^{-2}$

TABLE IV. QCD interference amplitudes $2\,\mathrm{Re}\,(\mathcal{A}_{\mathrm{NLO}}\mathcal{A}_{\mathrm{LO}}^*)$ for $u\bar{d} \to \bar{c}se^+\nu_e\mu^+\nu_\mu$ subprocess.

	$1/\epsilon^2$	$1/\epsilon$	Finite
I operator	$3.455808248747951 \times 10^{-3}$	$-1.006571544788643 \times 10^{-4}$	$-1.947046109412057 \times 10^{-3}$
Loop	$-3.455808251685664 \times 10^{-3}$	$1.006571546305143 \times 10^{-4}$	$-5.605259390551837 \times 10^{-3}$
I+loop	$-2.937712573203299 \times 10^{-12}$	$1.516500563242879 \times 10^{-13}$	$-7.552305499963894 \times 10^{-3}$

$$\overline{|\mathcal{A}_{\mathrm{LO}}^{u\bar{d}\to\bar{u}d}|}^2 = 1.240926153611845 \times 10^{-2},$$
$$\overline{|\mathcal{A}_{\mathrm{LO}}^{u\bar{d}\to\bar{c}s}|}^2 = 4.071278180896138 \times 10^{-3}. \tag{A1}$$

The interference amplitudes $2\,\mathrm{Re}\,(\mathcal{A}_{\mathrm{NLO}}\mathcal{A}_{\mathrm{LO}}^*)$ for the one-loop corrections (including counterterms) and the I-operator contribution as defined in Ref. [37] are given in Table III and Table IV. Here we use the following convention for the one-loop integrals, with $D = 4 - 2\epsilon$,

$$T_0 = \frac{\mu_R^{2\epsilon}\Gamma(1-\epsilon)}{i\pi^{2-\epsilon}} \int d^D q \frac{1}{(q^2 - m_1^2 + i0)\cdots}. \tag{A2}$$

This amounts to dropping a factor $(4\pi)^\epsilon/\Gamma(1-\epsilon)$ both in the virtual corrections and the I-operator. Moreover, the conventional dimensional-regularization method [35] with

$\mu_R = 80$ GeV is used. Changing from the conventional dimensional-regularization method to the dimensional reduction scheme induces a finite shift. This shift can be easily found by observing that the sum $|\mathcal{A}_{\mathrm{LO}}|^2 + 2\,\mathrm{Re}\,(\mathcal{A}_{\mathrm{NLO}}\mathcal{A}_{\mathrm{LO}}^*)$ must be unchanged as explained in Ref. [52]. Thus, the shift on $2\,\mathrm{Re}\,(\mathcal{A}_{\mathrm{NLO}}\mathcal{A}_{\mathrm{LO}}^*)$ is opposite to the shift on the Born amplitude squared, which in turn is given by the following change in the strong coupling constant, see e.g. Ref. [53],

$$\alpha_s^{\overline{\mathrm{DR}}} = \alpha_s^{\overline{\mathrm{MS}}}\left(1 + \frac{\alpha_s}{4\pi}\right). \tag{A3}$$

The shift on the I-operator contribution can easily be calculated using the rule given in Ref. [37].

[1] B. Jager, C. Oleari, and D. Zeppenfeld, J. High Energy Phys. 07 (2006) 015.
[2] B. Jager, C. Oleari, and D. Zeppenfeld, Phys. Rev. D **73,** 113006 (2006).
[3] G. Bozzi, B. Jager, C. Oleari, and D. Zeppenfeld, Phys. Rev. D **75,** 073004 (2007).
[4] B. Jager, C. Oleari, and D. Zeppenfeld, Phys. Rev. D **80,** 034022 (2009).
[5] A. Denner, L. Hosekova, and S. Kallweit, Phys. Rev. D **86,** 114014 (2012).
[6] F. Campanario, N. Kaiser, and D. Zeppenfeld, Phys. Rev. D **89,** 014009 (2014).
[7] V. Hankele and D. Zeppenfeld, Phys. Lett. B **661,** 103 (2008).
[8] F. Campanario, V. Hankele, C. Oleari, S. Prestel, and D. Zeppenfeld, Phys. Rev. D **78,** 094012 (2008).
[9] G. Bozzi, F. Campanario, V. Hankele, and D. Zeppenfeld, Phys. Rev. D **81,** 094030 (2010).
[10] G. Bozzi, F. Campanario, M. Rauch, H. Rzehak, and D. Zeppenfeld, Phys. Lett. B **696,** 380 (2011).
[11] G. Bozzi, F. Campanario, M. Rauch, and D. Zeppenfeld, Phys. Rev. D **84,** 074028 (2011).
[12] G. Bozzi, F. Campanario, M. Rauch, and D. Zeppenfeld, Phys. Rev. D **83,** 114035 (2011).
[13] K. Arnold et al., Comput. Phys. Commun. **180,** 1661 (2009); K. Arnold et al., arXiv:1207.4975.
[14] A. Lazopoulos, K. Melnikov, and F. Petriello, Phys. Rev. D **76,** 014001 (2007).
[15] T. Binoth, G. Ossola, C. Papadopoulos, and R. Pittau, J. High Energy Phys. 06 (2008) 082.
[16] U. Baur, D. Wackeroth, and M. M. Weber, Proc. Sci. RADCOR2009 (**2010**) 067 [arXiv:1001.2688].
[17] D. T. Nhung, L. D. Ninh, and M. M. Weber, J. High Energy Phys. 12 (2013) 096.
[18] T. Melia, K. Melnikov, R. Rontsch, and G. Zanderighi, J. High Energy Phys. 12 (2010) 053.
[19] T. Melia, K. Melnikov, R. Rontsch, and G. Zanderighi, Phys. Rev. D **83,** 114043 (2011).
[20] N. Greiner, G. Heinrich, P. Mastrolia, G. Ossola, T. Reiter, and F. Tramontano, Phys. Lett. B **713,** 277 (2012).
[21] F. Campanario, M. Kerner, L. D. Ninh, and D. Zeppenfeld, Phys. Rev. Lett. **111,** 052003 (2013).
[22] T. Gehrmann, N. Greiner, and G. Heinrich, Phys. Rev. Lett. **111,** 222002 (2013).
[23] S. Alioli, P. Nason, C. Oleari, and E. Re, J. High Energy Phys. 06 (2010) 043.
[24] T. Melia, P. Nason, R. Rontsch, and G. Zanderighi, Eur. Phys. J. C **71,** 1670 (2011).
[25] B. Jager and G. Zanderighi, J. High Energy Phys. 11 (2011) 055.
[26] G. Passarino and M. Veltman, Nucl. Phys. **B160,** 151 (1979).
[27] A. Denner and S. Dittmaier, Nucl. Phys. **B734,** 62 (2006).
[28] F. Campanario, J. High Energy Phys. 10 (2011) 070.
[29] T. Binoth, J. P. Guillet, G. Heinrich, E. Pilon, and C. Schubert, J. High Energy Phys. 10 (2005) 015.
[30] G. 't Hooft and M. Veltman, Nucl. Phys. **B153,** 365 (1979).

[31] Z. Bern, L. J. Dixon, and D. A. Kosower, Nucl. Phys. **B412**, 751 (1994).

[32] S. Dittmaier, Nucl. Phys. **B675**, 447 (2003).

[33] D. T. Nhung and L. D. Ninh, Comput. Phys. Commun. **180**, 2258 (2009).

[34] A. Denner and S. Dittmaier, Nucl. Phys. **B844**, 199 (2011).

[35] G. 't Hooft and M. Veltman, Nucl. Phys. **B44**, 189 (1972).

[36] M. S. Chanowitz, M. Furman, and I. Hinchliffe, Nucl. Phys. **B159**, 225 (1979).

[37] S. Catani and M. Seymour, Nucl. Phys. **B485**, 291 (1997).

[38] T. Hahn, Comput. Phys. Commun. **140**, 418 (2001).

[39] T. Hahn and M. Perez-Victoria, Comput. Phys. Commun. **118**, 153 (1999).

[40] H. Murayama, I. Watanabe, and K. Hagiwara, Report No. KEK-91-11, 1992.

[41] J. Alwall, P. Demin, S. de Visscher, R. Frederix, M. Herquet, F. Maltoni, T. Plehn, D. L. Rainwater, and T. Stelzer, J. High Energy Phys. 09 (2007) 028.

[42] K. Hagiwara and D. Zeppenfeld, Nucl. Phys. **B313**, 560 (1989).

[43] A. Sirlin, Nucl. Phys. **B192**, 93 (1981).

[44] F. Campanario, C. Englert, M. Rauch, and D. Zeppenfeld, Phys. Lett. B **704**, 515 (2011).

[45] F. Campanario, T. Figy, S. Platzer, and M. Sjodahl, Phys. Rev. Lett. **111**, 211802 (2013).

[46] A. Martin, W. Stirling, R. Thorne, and G. Watt, Eur. Phys. J. C **63**, 189 (2009).

[47] M. Cacciari, G. P. Salam, and G. Soyez, J. High Energy Phys. 04 (2008) 063.

[48] T. Gleisberg, S. Höche, F. Krauss, M. Schönherr, S. Schumann, F. Siegert, and J. Winter, J. High Energy Phys. 02 (2009) 007.

[49] T. Gleisberg and S. Hoeche, J. High Energy Phys. 12 (2008) 039.

[50] K. Mishra *et al.*, arXiv:1308.1430.

[51] S. D. Ellis, Z. Kunszt, and D. E. Soper, Phys. Rev. Lett. **69**, 1496 (1992).

[52] S. Catani, M. Seymour, and Z. Trocsanyi, Phys. Rev. D **55**, 6819 (1997).

[53] Z. Kunszt, A. Signer, and Z. Trocsanyi, Nucl. Phys. **B411**, 397 (1994).